Acta Mech 229, 3943–3962 (2018)
https://doi.org/10.1007/s00707-018-2211-6

ORIGINAL PAPER

A. Esmaeeli · Md. Abdul Halim

Electrohydrodynamics of a liquid drop in AC electric fields

Received: 12 January 2018 / Revised: 25 June 2018 / Published online: 31 July 2018

Abstract The aim of this study is to gain a detailed understanding of the behavior of a liquid drop in AC electric fields at finite Reynolds number. A front-tracking/finite difference method, in conjunction with Taylor–Melcher leaky dielectric model, is used to solve the governing electrohydrodynamic equations. The evolution of the flow field and the drop deformation are studied for three representative fluid systems, corresponding to the three regions of the deformation–circulation map. It is shown that for the range of the physical parameters used here, the relaxation time during which the drop settles to its quasi-steady-state deformation is essentially the same as that predicted by the creeping flow solution. Furthermore, the mean (time-independent) deformation is well represented by its steady-state deformation in the corresponding DC field in a root-mean-square sense. The evolution of the flow field shows formation of closed vortices that cross the drop surface and move toward the ambient fluid or the drop, in line with the motion of the drop surface. The evolution of the kinetic energy of the flow field with time is investigated, and the correlations between the minimum and the maximum kinetic energy and the state of the drop deformation are explored.

1 Introduction

When a liquid drop is exposed to an electric field, the mismatch between the dielectric properties of the drop and the suspending fluid results in electrical stresses at the drop surface that tend to deform the drop and set the fluid in motion. The phenomenon finds relevance in a host of microfluidic applications, where one can take advantage of the interfacial stresses as an action-from-the-distance force to manipulate the drop. Examples include breakup of drops in high-electric fields for surface coating and spraying [1], enhancement of coalescence of droplets for de-emulsification purposes [2], and manipulation of drops by electrowetting for digital microfluidic circuits [3].

The theoretical foundation of the phenomenon was laid out by Taylor and Melcher [4–6] in a framework that later on became known as "Taylor–Melcher leaky dielectric theory" [7]. The essence of the model is to assume that the droplet fluid and the host fluid have finite electric conductivities and that the time scale of charge relaxation due to conduction from the fluid bulk to the drop surface is much shorter than any process time of interest. The first assumption allows for the accumulation of free electric charges at the drop surface and, therefore, the possibility of a "net" interfacial electrical shear force, which results in fluid flow at the drop surface even when the drop is stationary and its surface is immobile. The second assumption leads to substantial simplification of the mathematical formulation as the electric field equations will be decoupled from the momentum equation and reduce to quasi-steady-state laws.

The steady behavior of a drop in a DC electric field is reasonably well understood. Briefly, under a weak electric field the drop remains spherical or deforms to an ellipsoid whose major axis is in the direction of or

A. Esmaeeli (✉) · Md. Abdul Halim
Southern Illinois University at Carbondale, Carbondale, USA
E-mail: esmaeeli@engr.siu.edu

perpendicular to the field, becoming a prolate or an oblate spheroid, respectively. Furthermore, a recirculatory flow in the form of toroidal vortices is established inside the drop that is matched with a corresponding flow in the ambient. The external flow resembles that of a uniaxial or biaxial flow, where it runs from the equator toward the poles or in the opposite direction. The key parameter that sets the sense of drop deformation and fluid flow circulation is the relative strength of the electric conductivity ratio $\widetilde{\sigma} = \sigma_i/\sigma_o$ and the electric permittivity ratio $\widetilde{\epsilon} = \epsilon_i/\epsilon_o$ (drop fluid/host fluid). This parameter is asserted in the deformation characteristic function $\Phi(\widetilde{\sigma}, \widetilde{\epsilon}, \widetilde{\mu})$ ($\widetilde{\mu}$ being the viscosity ratio) and the interfacial tangential velocity u_{θ_i}, which are used to determine the senses of drop deformation and fluid flow circulation [8–10]. The expected shape of the drop and the flow pattern are typically presented by the so-called deformation–circulation map, which is constructed by plotting the zero-deformation curve $\Phi = 0$ and the zero-circulation line $u_{\theta_i} = 0$ together in an $\widetilde{\epsilon} - \widetilde{\sigma}$ coordinate.

While a DC electric field provides a robust means for manipulation of the drops, in many cases the use of an AC electric field proves to be more advantageous. For instance, in experimental studies to characterize the deformation of a stationary solitary drop, the drop will move toward one of the electrodes because of electrophoresis, when it acquires a small net electric charge. The electrophoresis, however, can be eliminated in an AC field by adjusting the frequency [8]. As such, a number of notable experimental studies to determine the steady-state deformation of a drop under a DC electric field have been performed using an AC electric field, by considering an effective field strength that was equal to that of the uniform DC field in a root-mean-square (rms) sense. See, for example, Refs. [8,11–13]. Similarly, in continuous flow electrophoresis (CFE), which is a preparative technique that is used in health industry to prepare large quantities of protein and pure biological materials (by application of a DC electric field perpendicular to the axis of a jet stream that contains the biological sample), Limat et al. [14] showed that the use of an AC field whose direction is perpendicular to both the jet axis and the DC electric field will mitigate the customary problem of sample degradation (the so-called ribbon effect) during the process and, thereby, improve the quality of the product.

Despite the proven impact and the potential applications of AC electric fields in manipulation of liquid drops, the number of studies in this regard is much more limited than those of the DC fields. Here, the theoretical foundation of the problem was first laid out by Torza et al. [8], who considered a drop, in an unbounded domain, exposed to an electric field strength of the form $\mathbf{E}_{\text{ext}}(t) = \mathbf{E}_0 \cos \omega t$, and solved the axisymmetric creeping flow equations in conjunction with the Laplace equation for the electric potential. In doing so, the authors ignored the convective term $\rho \mathbf{u} \cdot \nabla \mathbf{u}$ and the local acceleration term $\rho \partial \mathbf{u}/\partial t$ in the momentum equation. Accordingly, they were able to find a closed form analytical solution for the problem. The results of this study showed that the net interfacial normal $[\![\tau_{nn}^e]\!]$ and tangential $[\![\tau_{nt}^e]\!]$ electric stresses, the velocity field $\mathbf{u}$, and the deformation $\mathcal{D}$ could be written as a sum of a mean (time-independent) part $\mathcal{R}_m$, which was a function of the field frequency (in addition to other controlling parameters) and a time-periodic part $\mathcal{R}_{tp}$, whose circular frequency was twice that of the frequency of the applied field,

$$\mathcal{R} = \mathcal{R}_m + \mathcal{R}_{tp}. \tag{1}$$

Here $\mathcal{R}$ represents one of $[\![\tau_{nn}^e]\!]$, $[\![\tau_{nt}^e]\!]$, $\mathbf{u}$, and $\mathcal{D}$. For $\omega = 0$, their mean (time-independent) deformation $\mathcal{D}_m$ converged to that of the Taylor steady-state solution [15] for a leaky dielectric drop in a DC electric field [15], provided they used

$$E_{\text{rms}} = \lim_{T \to \infty} \sqrt{\frac{1}{2T} \int_{-T}^{T} (E_0 \cos \omega t)^2 \mathrm{d}t} \equiv \frac{E_0}{\sqrt{2}}, \tag{2}$$

in lieu of E_0 in the Taylor's solution. On the other hand, for high frequency ($\omega \to \infty$), their mean deformation $\mathcal{D}_m$ converged to that of Allan and Mason's steady-state solution [16] for a perfect dielectric drop in a DC electric field, provided they used E_{rms} in lieu of E_0 in Allan and Mason's solution. This is intuitively understandable, since at high frequency the time scale of charge migration from the fluid bulk to the surface ϵ/σ is much larger than the time scale of the change of the polarity of the electrodes $1/\omega$, and therefore, the fluid system behaves as a perfect dielectric. The authors also determined the range of fluid property ratios $(\widetilde{\sigma}, \widetilde{\epsilon}, \widetilde{\mu})$ and frequencies (ω) for which the mean drop shape would be oblate, prolate, or spherical, by examining the sign of the mean deformation characteristic function $\Phi_m = f(\widetilde{\sigma}, \widetilde{\epsilon}, \widetilde{\mu}; \omega)$. Accordingly, they categorized the fluid systems into three different classes (or regions) based on the signs of Φ_m and its derivative $\partial \Phi_m/\partial \omega$, which are the same as the signs of $\mathcal{D}_m$ and $\partial \mathcal{D}_m/\partial \omega$, respectively, $\mathcal{D}_m$ being the mean deformation. As it turned out, the effect of ω on the mean deformation $\mathcal{D}_m$ was mixed; for some fluid systems the mean deformation increased with an increase in the frequency ($\partial \mathcal{D}_m/\partial \omega > 0$), while for some others the opposite was true ($\partial \mathcal{D}_m/\partial \omega < 0$). For one of the fluid classes, they also identified a critical frequency ω_{cr} at which the mean drop shape remained spherical ($\mathcal{D}_m = 0$) regardless of the field strength.

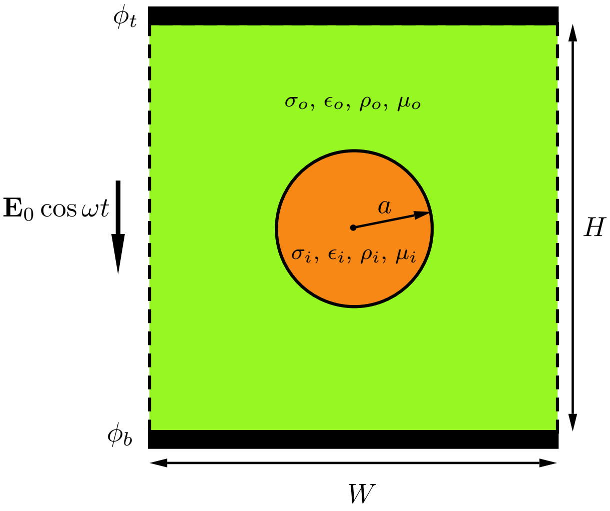

Fig. 1 Computational setup depicting a liquid drop of radius a immersed in another liquid. Here ρ, μ, σ, and ϵ represent, respectively, the density, the viscosity, the electric conductivity, and the electric permittivity. The computational domain is wall-bounded in the vertical direction and periodic in the horizontal direction

Sozou [17] followed Torza's et al. study [8] by improving their solution, accounting for the local acceleration term $\rho \partial \mathbf{u}/\partial t$ in the momentum equation. He showed that overlooking this term for fluids of low viscosity or fields of high frequency can lead to inaccurate results, qualitatively and quantitatively. Not many theoretical studies seem to have been performed about this problem in the intervening period between the publication of Sozou's work and the turn of the century. In recent years, however, there has been a resurgence of interest on the subject, driven by its potential applications. Here, a noteworthy study is due to Ref. [18], who found an analytical solution concerning the behavior of a drop in a nonuniform AC electric field under creeping flow condition.

The analytical solutions of Torza et al. [8] and Sozou [17] provide a solid theoretical basis regarding the quasi-steady (time-periodic) state. However, no attempt has been made so far to explore the dynamics of the drop and the evolution of the flow field in the transient period. Furthermore, the restrictive assumptions of creeping flow and small deformation, used in these studies, limit their range of applicability to a smaller subset of fluid systems, imposed electric field strengths, and drop sizes. The aim of this study is to relax those restrictions and shed some light on the less explored aspects of the problem, using direct numerical simulations. While the computations are performed for two-dimensional systems, the results are applicable to the actual three-dimensional systems in a "qualitative" sense. They also find relevance in applications involving the interaction of an AC electric field with a liquid jet or column, where the direction of the field is transverse to the jet axis [19–21].

2 Problem setup and nondimensional parameters

The problem setup is shown in Fig. 1, depicting an initially circular drop in a pool of another liquid, confined in a channel. The electric field is established by earthing the bottom wall and assigning an oscillatory electric potential to the top wall,

$$\phi(x, 0, t) \equiv \phi_b = 0; \quad \phi(x, H, t) \equiv \phi_t = \phi_0 \cos \omega t, \tag{3}$$

where ϕ_0 is the field amplitude and $\omega = 2\pi\nu$ is the angular frequency of the field, ν being the frequency. Thus, in the absence of the drop, the imposed electric field strength is

$$\mathbf{E}_{\text{ext}} = E_0 \hat{j} \cos \omega t \tag{4}$$

where $E_0 = \phi_0/H$. The computational domain is periodic in the horizontal direction and wall-bounded in the vertical direction. No-slip and no-through flow boundary conditions are used for the velocity field at the walls, and periodic boundary conditions are used in the horizontal direction.

The physical properties of the fluids are the densities, ρ_i, ρ_o, the viscosities, μ_i, μ_o, the electric permittivities, ϵ_i, ϵ_o, and the electric conductivities, σ_i, σ_o. The surface tension is γ. The subscripts i and o denote inside and outside of the drop. Buoyancy is ignored by considering density-matched fluids, $\rho_i = \rho_o$. The governing nondimensional numbers of this problem are

$$Oh = \frac{\mu_o}{\sqrt{\rho_o a \gamma}}, \quad E^* = \frac{E_0}{\sqrt{\gamma/\epsilon_o a}}, \quad Re_\omega = \frac{\rho_o \omega a^2}{\mu_o}, \quad \alpha = \frac{\pi a^2}{WH}, \tag{5.1}$$

$$\widetilde{\sigma} = \frac{\sigma_i}{\sigma_o}, \quad \widetilde{\epsilon} = \frac{\epsilon_i}{\epsilon_o}, \quad \widetilde{\rho} = \frac{\rho_i}{\rho_o}, \quad \widetilde{\mu} = \frac{\mu_i}{\mu_o}, \tag{5.2}$$

where Oh is the Ohnesorge number, E^* is the nondimensional strength of the electric field, Re_ω is the Reynolds number based on the oscillatory velocity scale $a\omega$, and α is the area fraction. Sometimes in the literature, the flow Reynolds number $Re_f = \rho_o u_s a/\mu_o$ and the capillary number $Ca_f = \mu_o u_s/\gamma \equiv E^{*2}$ are used in lieu of Oh and E^*, respectively, where $u_s = \epsilon_o E_0^2 a/\mu_o$ is the electrohydrodynamic velocity scale.

For the leaky dielectric model to be valid, the time scale of charge relaxation from the fluid bulk to the surface of the drop

$$\tau_C = \max(\tau_{C_i}, \tau_{C_o}), \tag{6.1}$$

$$\tau_{C_i} = \frac{\epsilon_i}{\sigma_i}, \quad \tau_{C_o} = \frac{\epsilon_o}{\sigma_o} \tag{6.2}$$

should be much shorter than any process time of interest τ_P. The ratio of τ_C to τ_P is called the electric Reynolds number $Re_{el} = \tau_C/\tau_P$, and thus, it should be very small. In this study, the time scale that it takes for the drop deformation to settle to its quasi-steady state $\mu a/\gamma$ is considered the process time of interest; thus, $Re_{el} = \epsilon\gamma/\sigma\mu a$, which is sufficiently small (i.e., $Re_{el} = 0.02$). For all the simulations performed in this study, the computational domain was $2.5d \times 2.5d$ (d being the initial diameter of the drop), which was resolved by a 256×256 grid. A grid refinement study showed that this grid resolution leads to essentially grid-independent results.

3 Mathematical formulation and numerical method

The mathematical formulation of the problem is based on the so-called one-fluid formulation, where a single set of equations are used to represent both fluids and the jump conditions are enforced using smoothed delta functions that are added to the governing equations. The numerical method is based on the front-tracking/finite difference technique, where in addition to a regular fixed grid a moving unstructured grid is also used to explicitly track the interface. The governing equations are solved in conjunction with the Taylor–Melcher leaky dielectric theory. Detailed information about the numerical method, in the absence of the electric field, can be found in the review article by Tryggvason et al. [22], and the modification of the method to account for the electrohydrodynamic forces can be found in Refs. [23,24].

In the numerical solution of the electric field equations, we find the electric potential ϕ by solving a self-adjoint equation, $\nabla \cdot \sigma \nabla \phi = 0$. This equation recovers the Laplace equations inside and outside of the drop, $\nabla^2 \phi_i = 0$ and $\nabla^2 \phi_o = 0$, and satisfies the jump conditions (i) $\phi_i = \phi_o$ and (ii) $\sigma_i \partial\phi_i/\partial n = \sigma_o \partial\phi_o/\partial n$ at the interface. Since the second jump condition is an approximation of the more general equation of the conservation of surface charge at the free surface [24], this approximation will be reasonable only if $\Pi = \tau_C/\tau_{\min} \ll 1$, where $\tau_{\min} = \min(\tau_{\text{conv}}, \tau_{\text{diff}}, \tau_{\text{def}}, \tau_e)$. Here

$$\tau_{\text{conv}} = \frac{a}{u_s}, \quad \tau_{\text{diff}} = \frac{a^2}{\nu}, \quad \tau_{\text{def}} = \frac{\mu_o a}{\gamma}, \quad \tau_e = \frac{1}{\omega}$$

are, respectively, the convective, the momentum diffusion, the deformation or capillary, and the electric field time scales. In all of our simulations, $\tau_{\text{conv}} = 4$, $\tau_{\text{diff}} = 4$, $\tau_e = 1$, and $\tau_{\text{def}} = 1$. Thus, $\tau_{\text{def}} \equiv \tau_e = 1$ is the minimum time scale. For the simulations in Sects. 5.2–5.4, respectively, ($\tau_{C_i} = 0.08$, $\tau_{C_o} = 0.02$), ($\tau_{C_i} = 0.0333$, $\tau_{C_o} = 0.02$), and ($\tau_{C_i} = 0.0067$, $\tau_{C_o} = 0.02$). Thus, $\Pi = \epsilon\omega/\sigma$ is reasonably small. It should be noted, however, that this restriction imposes a limitation on the upper range of the electric frequencies that we can use in our simulations.

In passing, we should mention that the effects of surface charge convection $\nabla \cdot (q_s \mathbf{u})$ and charge buildup $\partial q_s/\partial t$ in the context of a DC electric field have been explored by several authors [25–27]. The results of these studies show that accounting for the charge buildup can lead to a nonmonotonic deformation–time history curve and that the droplet and medium behave as perfect dielectrics at early times, which always favors an initial prolate deformation. Furthermore, the main effect of charge convection is to reduce the interfacial velocity, leading oblate drops to deform less, but prolate drops to deform more.

4 Background

The key parameters that determine the sense of drop deformation and fluid circulation are the net normal $[\![\tau^e_{nn}]\!]$ and tangential $[\![\tau^e_{nt}]\!]$ electric forces at the interface. Here, the double bracket denotes the jump in a physical parameter across the interface (outside minus inside). Using the Maxwell stress tensor $\boldsymbol{\tau}_M = \epsilon \mathbf{EE} - (1/2)\epsilon \mathbf{IE}\cdot\mathbf{E}$ it can be shown that

$$[\![\tau^e_{nn}]\!] = \frac{1}{2}\epsilon_o \left[E^2_{n_o} - \widetilde{\epsilon} E^2_{n_i} - (1-\widetilde{\epsilon})E^2_t\right] \tag{7}$$

and

$$[\![\tau^e_{nt}]\!] = \epsilon_o E_t \left(E_{n_o} - \widetilde{\epsilon} E_{n_i}\right) \equiv q_s E_t \tag{8}$$

where

$$q_s = \epsilon_o \left(E_{n_o} - \widetilde{\epsilon} E_{n_i}\right) \tag{9}$$

is the free electric charge at the surface. In the above equations, the electric strengths (E_t, E_{n_i}, and E_{n_o}) are evaluated at the interface. Here, the electric stresses are presented in terms of normal–tangent $n-t$ coordinates so that they can be used for a general orthogonal coordinate system. Subscripts "i" and "o" stand for the inside and outside, and $E_{t_i} = E_{t_o} \equiv E_t$. For a spherical (circular) drop in three (two)-dimensional spherical (polar) coordinates, $n \equiv r$ and $t \equiv \theta$. Both components of the electric field contribute to the net normal and tangential electric stresses. The normal electric stress is due to both the polarization charge and the free surface charge. As such, it is nonzero in perfectly dielectric fluid systems, where the surface charge is zero. The tangential electric stress, however, arises only in leaky dielectric fluid systems as a result of action of the electric field on the free surface charge. Thus, when the surface charge q_s or the tangential component of the electric field E_t is null, this term is zero. E_t could become vanishingly small when $\widetilde{\sigma} \gg 1$.

As shown by Torza et al. [8] and Esmaeeli and Halim [28], for a three- and a two-dimensional liquid drop, respectively, the net electrical stresses ($[\![\tau^e_{nn}]\!]$, $[\![\tau^e_{nt}]\!]$) comprise a mean and a time-periodic component with a frequency of 2ω. Since these stresses are the driving forces of the problem, the drop deformation and velocity field will also comprise a mean and a time-periodic component, i.e., $\mathcal{D} = \mathcal{D}_m + \mathcal{D}_{tp}$ and $\mathbf{u} = \mathbf{u}_m + \mathbf{u}_{tp}$. Furthermore, both $\mathcal{D}_{tp}$ and $\mathbf{u}_{tp}$ will have a phase difference with respect to the imposed electric field, Eq. (4).

For a slightly deformed drop the deformation is typically defined as

$$\mathcal{D} = \frac{y_{\max} - x_{\max}}{y_{\max} + x_{\max}} \tag{10}$$

where $y_{\max}$ and $x_{\max}$ are the end-to-end length of the drop in the direction of electric field and the maximum breadth in the transverse direction, respectively. For two-dimensional systems, the mean deformation $\mathcal{D}_m$ is [28]

$$\mathcal{D}_m = \frac{1}{6} Ca_f \Phi_m, \tag{11.1}$$

$$\Phi_m = 1 - \frac{\widetilde{\sigma} + \widetilde{\epsilon}(3 + 4\Pi^2)}{(\widetilde{\sigma}+1)^2 + \Pi^2(\widetilde{\epsilon}+1)^2} \tag{11.2}$$

where $Ca_f \equiv E^{*2} = \epsilon_o a E_0^2/\gamma$, $\Pi = \epsilon_o \omega/\sigma_o \equiv \tau_{C_o}/\tau_e$, and Φ_m is the deformation characteristic function, which determines the sense of drop deformation. For comparison, we also report the deformation parameter in a steady-state DC electric field

$$\mathcal{D}_0 = \frac{1}{3} Ca_f \Phi_0, \tag{12.1}$$

$$\Phi_0 = \frac{\widetilde{\sigma}^2 + \widetilde{\sigma} + 1 - 3\widetilde{\epsilon}}{(\widetilde{\sigma}+1)^2}. \tag{12.2}$$

For $\omega = 0$, the mean deformation characteristic function converges to that of a leaky dielectric fluid system in a DC electric field, $\Phi_m = \Phi_0$, and the mean deformation $\mathcal{D}_m$ will be the same as the deformation in the DC field $\mathcal{D}_0$, provided $E_{\text{rms}} = E_0/\sqrt{2}$ is used in lieu of E_0 in evaluating $\mathcal{D}_0$. On the other hand, for $\omega \to \infty$, $\mathcal{D}_m$ will converge to the deformation of a perfect dielectric drop (i.e., $\widetilde{\epsilon} = \epsilon_i/\epsilon_o$, $\sigma_i = \sigma_o = 0$) in a DC field,

$$\mathcal{D}_{0_{PD}} = \frac{1}{3} Ca_f \Phi_{0_{PD}}, \tag{13.1}$$

$$\Phi_{0_{PD}} = \left(\frac{\widetilde{\epsilon} - 1}{\widetilde{\epsilon} + 1}\right)^2, \tag{13.2}$$

provided $E_{\text{rms}} = E_0/\sqrt{2}$ is used in lieu of E_0 in evaluating $\mathcal{D}_{0_{PD}}$.

To study the behavior of a liquid drop in AC fields, it will be quite helpful to predict its mean behavior using the so-called deformation–circulation map. This map is constructed by drawing the zero-deformation curve $\Phi_0 = 0$ and the zero-circulation line $\widetilde{\sigma} = \widetilde{\epsilon}$ together in a $\widetilde{\sigma} - \widetilde{\epsilon}$ coordinate, corresponding to the steady-state behavior of a drop in a DC field, and it was initially used by Torza et al. [8] to help analyze their experimental and analytical results in AC fields. Although the building blocks of the map are based on a DC field, the map represents the mean behavior of the drop in an AC field, since for a given fluid system (i.e., given $\widetilde{\sigma}$ and $\widetilde{\epsilon}$) $\Phi_0 = 0$ implies $\Phi_m = 0$, and the sense of mean flow circulation for an AC field is the same as the sense of steady-state circulation in the corresponding DC field. However, here, once the map is made, the effect of the frequency ω on each region of the map needs to be accounted for. Figure 2 shows the map for a drop in the two-dimensional system, which is the same as that in Ref. [29]. Here the straight line is the so-called zero-circulation line, where $\widetilde{\epsilon} = \widetilde{\sigma}$. Along this line, the mean velocity field $\mathbf{u}_m$ is zero, since $\widetilde{\epsilon} = \widetilde{\sigma}$ is tantamount to a perfect dielectric fluid system. The $\Phi_0 = 0$ curve is the so-called zero-deformation curve, along which $\widetilde{\sigma}^2 + \widetilde{\sigma} + 1 - 3\widetilde{\epsilon} = 0$. The $\Phi_0 = 0$ curve and the $\widetilde{\epsilon} = \widetilde{\sigma}$ line divide the domain into three regions, according to the sense of mean deformation of the drop (prolate versus oblate) and the direction of the mean external flow (poles-to-equator versus equator-to-poles). Here, a prolate or an oblate ellipse is defined, respectively, as an ellipse with its major axis in the direction of or perpendicular to the field. In region **I**, $\widetilde{\sigma} < \widetilde{\epsilon}$, and there exists a critical frequency [28]

$$\omega_{\text{cr}} = \frac{\sigma_o}{\epsilon_o} \frac{\sqrt{3\widetilde{\epsilon} - 1 - \widetilde{\sigma} - \widetilde{\sigma}^2}}{|\widetilde{\epsilon} - 1|} \tag{14}$$

above and below which the drop deforms to a prolate or an oblate ellipse, respectively, i.e., for $\omega > \omega_{\text{cr}}$, $\mathcal{D}_m > 0$, and for $\omega < \omega_{\text{cr}}$, $\mathcal{D}_m < 0$. At $\omega = \omega_{\text{cr}}$, the drop remains circular ($\mathcal{D}_m = 0$), regardless of the strength of the field. Here, the mean (time-independent) external fluid flows from the top/bottom (poles) toward the sides (equator). Furthermore, the mean deformation increases with an increase in the frequency, $\partial \mathcal{D}_m/\partial\omega > 0$. In region **II**, $\mathcal{D}_m > 0$ and $\widetilde{\sigma} < \widetilde{\epsilon}$. Here, the drop deforms to a prolate ellipse, and the mean external fluid flows from the poles toward the equator. Furthermore, $\partial \mathcal{D}_m/\partial\omega > 0$. Finally, in region **III**, $\mathcal{D}_m > 0$, and $\widetilde{\sigma} > \widetilde{\epsilon}$. Here, the drop deforms to a prolate ellipse and the mean external fluid flows from the equator toward the poles. Furthermore, $\partial \mathcal{D}_m/\partial\omega \le 0$.

5 Results and discussion

Our aim is to investigate the evolution of the drop shape and the flow field in AC electric fields for representative fluid systems from the three regions of the deformation–circulation map. To this end, we have performed a simulation for each region. With the exception of $\widetilde{\sigma}$ and $\widetilde{\epsilon}$, which changes from one region to the other, the rest of the nondimensional input data, Oh (Re_f), E^* (Ca_f), α, $\widetilde{\rho}$, $\widetilde{\mu}$, are the same for all the simulations. Table 1 shows the nondimensional input data. To put the results of the AC electric field in perspective, we start our analysis by considering the steady-state behavior of a drop in a DC electric field. The input data for these simulations are the same as those for the corresponding AC fields, except that the electric potential of the top electrode was fixed at $\phi_t = \phi_{\text{rms}} \equiv \phi_0/\sqrt{2}$, ϕ_{rms} being the rms electric potential. The coordinates of the fluid systems used for these simulations are denoted, respectively, by a circle, a diamond, and a triangle, in the deformation–circulation map.

Figure 3 shows the velocity vectors, contours of electric potential, and the drop at a steady-state time for these cases. For the first case [frame (*a*)], $\widetilde{\sigma} = 2 < \widetilde{\epsilon} = 8$ and $\Phi_0 = -17 < 0$, so the expectation is that the drop becomes oblate and the external flow runs from the top and the bottom toward the sides. This is actually

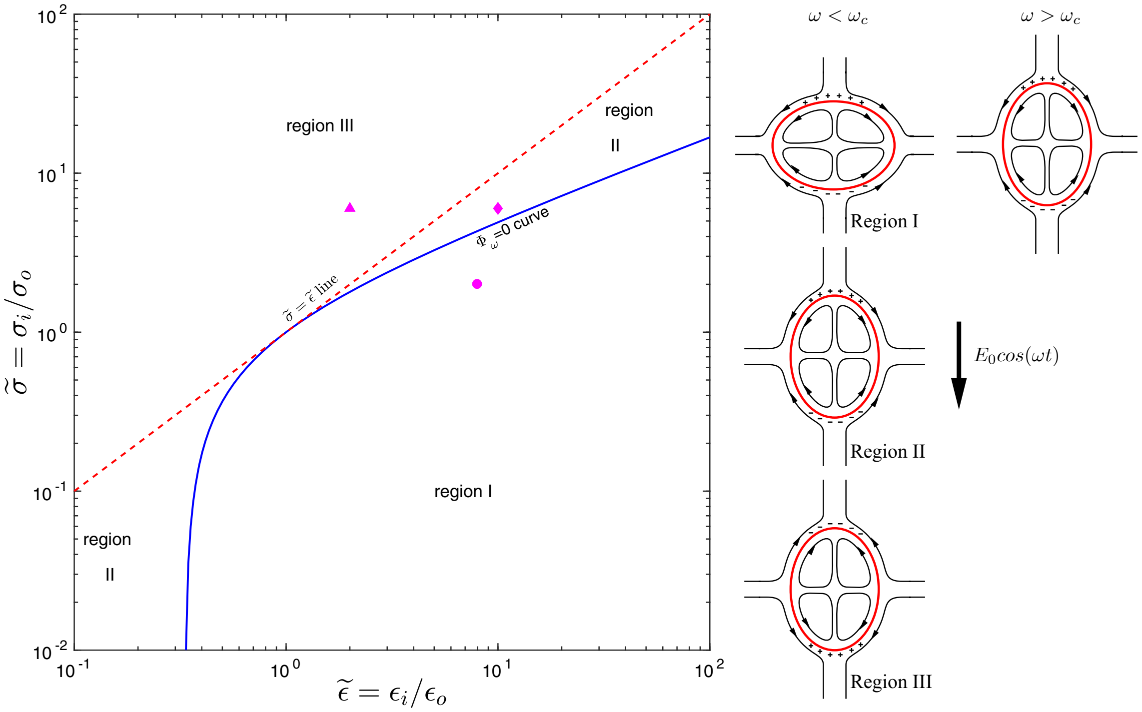

Fig. 2 Deformation–circulation map along with the schematics of the mean (time-independent) component of the flow pattern and modes of drop deformation. The coordinates of the fluid systems used in each region are $\widetilde{\epsilon} = 8$, $\widetilde{\sigma} = 2$ (circle; region **I**), $\widetilde{\epsilon} = 10$, $\widetilde{\sigma} = 6$ (diamond; region **II**), and $\widetilde{\epsilon} = 2$, $\widetilde{\sigma} = 6$ (triangle; region **III**)

Table 1 Magnitude of the nondimensional numbers used for the representative fluid systems in regions **I**–**III** of the map

Field	Oh (Re_f)	E^* (Ca_f)	Re_ω	α	$\widetilde{\rho}$	$\widetilde{\mu}$
DC	0.5 (0.5)	0.3536 (0.125)	0	0.1256	1	1
AC	0.5 (0.5)	0.50 (0.25)	4	0.1256	1	1

Region	$\widetilde{\sigma}$	$\widetilde{\epsilon}$
I	2	8
II	6	10
III	6	2

what is seen here. The steady-state velocity field consists of four closed vortices inside the drop that are matched by their counterparts in the outside. The fact that no velocity vector crosses the drop implies that the interface deformation has settled to a steady state. The steady-state deformation can be estimated from the creeping flow solution [30] which results in $\mathcal{D}_0 = -0.078$. For the second simulation [frame (b)], $\widetilde{\sigma} = 6 < \widetilde{\epsilon} = 10$ and $\Phi_0 = 13 > 0$. Here, the drop becomes prolate, $\mathcal{D}_0 = 0.011 > 0$, but there is no change in the direction of the velocity field. Finally, for the third simulation [frame (c)], $\widetilde{\sigma} = 6 > \widetilde{\epsilon} = 2$ and $\Phi_0 = 37 > 0$. Here, the drop becomes prolate, $\mathcal{D}_0 = 0.031 > 0$, and the direction of the external field is opposite to that for the previous two cases.

5.1 Evolution of the velocity field and the drop shape in AC electric fields

Here, the main focus is on the quasi-steady state, where the drop oscillates around a mean shape. Therefore, the snapshots of the velocity field and the drop are chosen at selected times within a cycle of the drop oscillation in that state, as identified in Fig. 4. In the analysis of the results, we will refer to the time interval in which the drop deformation increases from its minimum to its maximum as the "deformation period" or the "deformation half-cycle," and the time interval in which the drop deformation decreases from its maximum to its minimum as the "rebound period" or the "rebound half-cycle."

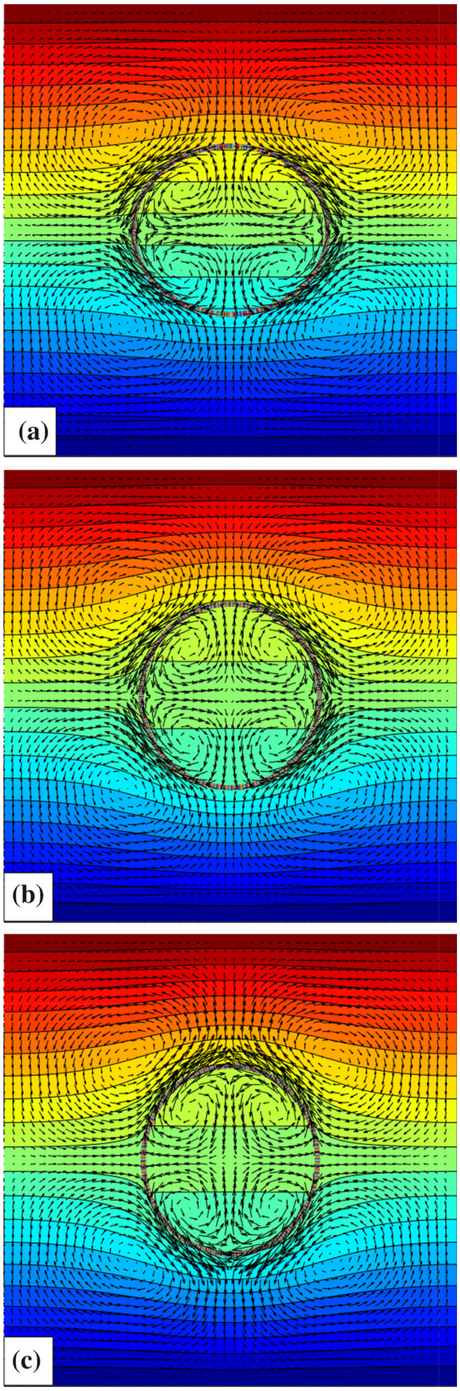

Fig. 3 Vector plot of the velocity field (at every fifth grid point) along with contours of the electric potential and the drop at a steady-state time, pertaining to a DC electric field and fluid systems from regions **I** (frame (a)), **II** (frame (b)), and **III** (frame (c))

5.2 Region **I** of the map

In this region, the sense of mean deformation depends on the field frequency ω being above or below a critical frequency ω_{cr}. Here, the frequency is $\omega = 1$ rad/s, which is less than the critical frequency $\omega_{\mathrm{cr}} = 29.45$, according to Eq. (14). Thus, we expect the drop to deform to an oblate ellipse. Furthermore, since $\widetilde{\sigma} < \widetilde{\epsilon}$, we expect the mean (time-independent) external fluid to flow from the poles toward the equator.

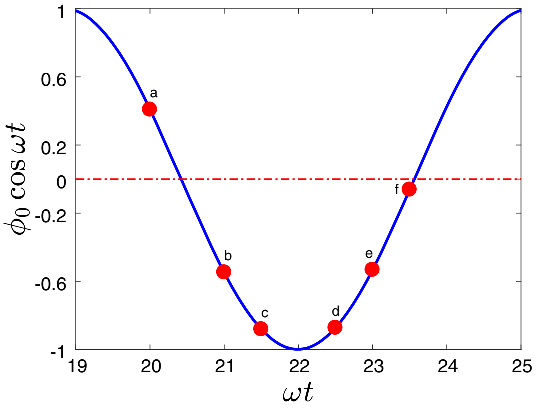

Fig. 4 Variation of the electric potential at the top electrode, $\phi_t = \phi_0 \cos \omega t$, with time. The solid circles mark ϕ_t at the times that correspond to the times of the velocity snapshots, i.e., $t = 20$, 21, 21.5, 22.5, 23, and 23.5

Figure 5 shows the deformation–time history, where we have marked the $\mathcal{D} - t$ and $\phi_t - t$ curves by solid circles and solid squares, respectively. Here, the mean drop shape is oblate (i.e., $\mathcal{D} < 0$). Thus, the maxima and the minima on the graph correspond to the minimum and maximum deformations, respectively. The drop goes through a transient period before it reaches the quasi-steady state, where the drop oscillates around its mean with frequency of 2ω. This relaxation time is not accounted for in the analytical solution of Torza et al. [8], since their solution is valid for times that are sufficiently larger than the transient time. While Sozou [17] accounted for it in his mathematical formulation, unfortunately, it is not possible to discern any information about it, since his solution is not in a closed form. The end of the transient period marks the beginning of the quasi-steady state, where the drop oscillates around its time-independent (mean) deformation $\mathcal{D}_m$. Markers (a)–(c) reside in the rebound half-cycle, while markers (d)–(f) reside in the deformation half-cycle.

The transient time can be estimated from the analytical solution of Ref. [31] who studied the deformation of a two-dimensional drop in a uniform DC electric field, assuming $Re_f \ll 1$ and $Oh^2 \gg 1$, and found that

$$\mathcal{D}(t) = \mathcal{D}_0 \left[1 - \exp\left(-\frac{t}{\tau} \right) \right], \tag{15.1}$$

$$\tau = \frac{(\mu_i + \mu_o)a}{\gamma}, \tag{15.2}$$

where $\tau \equiv \tau_{DC}$ is the deformation relaxation time and $\mathcal{D}_0$ is the steady-state deformation, given by Eq. (12). To evaluate the transient time, we have added the result of the prediction of Eq. (15) to the Figure. Comparison of the analytical result and the numerical result for the DC field shows that the transient time for the latter is approximately the same as that for the former. Since the $\mathcal{D} - t$ curve for the DC field represents well the evolution of the mean deformation in the AC field, it can be conjectured that the transient time for the deformation of the drop in the AC field, τ_{AC}, is essentially the same as that predicted by Eq. (15). The success of Eq. (15) in predicting the transient time is surprising, considering the fact that in the numerical simulation $Re_f = 0.5$ and $Oh^2 = 0.25$, which are outside the realm of the validity of this equation. We also note that the analytical solution underpredicts the degree of deformation, which is presumably due to the inertia and/or the confinement effects [32] that exist in the simulations, but are absent in the analytical solution. This point will be explored in Sect. 6.

In the experimental studies of the problem, a high-frequency (i.e., 60 Hz or so) AC field has been generally used to explore the behavior of a perfectly dielectric liquid drop in a DC field [8,11–13]. Here the mean (time-independent) deformation of the drop under an electric field strength of E_0 is perceived as its deformation in a DC electric field of strength $E_0/\sqrt{2}$; see Sect. 4. Since at $\omega = 0$, $\mathcal{D}_m = \overline{\mathcal{D}}_0$ (the overbar signifies that E_{rms} is used in evaluating Eq. (12)), it is conceivable that this will also hold at low frequencies. To explore this issue, we have added the deformation from the corresponding DC simulation to the Figure. As is evident, the deformation curve for the DC simulation passes through the midpoints between the maxima and the minima of the AC deformation curve. Accordingly, this undertaking seems to be justifiable in predicting the steady deformation for the current simulation.

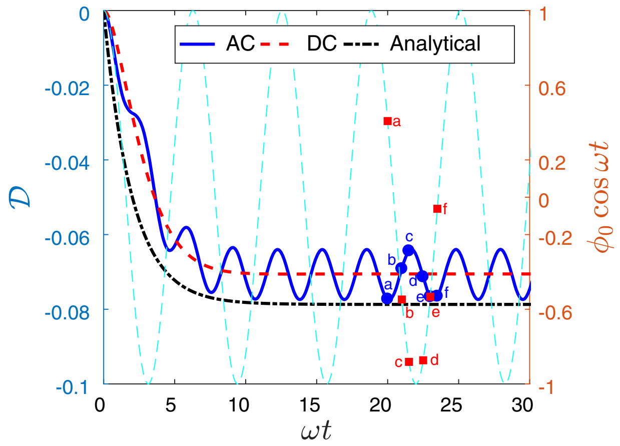

Fig. 5 Evolution of the deformation parameter $\mathcal{D}$ with time, pertaining to the representative simulation in region **I**. The red dashed line represents $\mathcal{D} - t$ for the corresponding DC field simulation. The dashed-dotted line is based on Eq. (15). The solid circles and squares mark the $\mathcal{D} - t$ and $\phi_t - t$ curves, respectively, at the times that correspond to the times of the velocity snapshots

We now turn our attention to the velocity field. Figure 6 shows the velocity vectors along with the contours of the electric potential and the drop at the selected times corresponding to markers in Figs. 4 and 5. Here $\widetilde{\sigma} = 2 < \widetilde{\epsilon} = 8$; thus, it is expected that the mean external flow runs from the poles toward the equator. The velocity field for the first frame is similar to that for the steady-state DC electric field (Fig. 3a); the external flow runs from the top and the bottom toward the sides. Here, however, the vectors cross the interface because the time of frame (a) is not chosen exactly at the time that the deformation is maximum (i.e., $\partial \mathcal{D}/\partial t = 0$). The net electric stresses lead to the net tangential $[\![\tau^h_{nt}]\!]$ and normal $[\![\sigma^h_{nn}]\!] \equiv [\![\tau^h_{nn}]\!] - [\![p]\!]$ hydrodynamic stresses. The former leads to a formation of closed vortices in and around the drop that do not cross its surface, since this stress does not contribute to the drop deformation. On the other hand, the latter leads to streamlines that cross into the drop from the poles and exit from the equator (or vice versa, depending on the direction of the flow field), and contributes to the drop deformation. The overall flow field is the result of the interplay of the flow generated by these two stresses. Here, we refer to the flow driven by $[\![\tau^h_{nt}]\!]$ as the shear-driven flow and that due to $[\![\sigma^h_{nn}]\!]$ as the deformation-driven flow. When the rate of the deformation is zero (at the minima and maxima of the $\mathcal{D} - t$ curve), the flow is solely driven by $[\![\tau^h_{nt}]\!]$. As such, the flow pattern is the same as that of a steady-state uniform DC field. However, the flow strength is not the same as that in the DC field. To analyze the change in the flow pattern with time, it will be quite helpful to consider simultaneously the velocity field and the deformation–time history. In frames (a)–(c), which reside in the rebound half-cycle, the fluid moves outward near the poles and inward near the equator, in line with the direction of motion of the drop surface. The flow direction is reversed in the deformation half-cycle [frames (d)–(e)], in line with the reversal of the direction of motion of the drop surface. The cycle is repeated as can be seen from the direction of the flow field in frame (f), which resides in the subsequent rebound half-cycle.

A few comments regarding the recent observations are in order. First, the reversal of the direction of the velocity vectors and/or the rate of the deformation ($\partial \mathcal{D}/\partial t \lessgtr 0$) has nothing to do with the change in the polarity of the electrodes. This is because these quantities are proportional to E_0^2, according to Eqs. (7) and (8). Second, the maximum deformation (i.e., minima in the curve) does not correspond to the maximum field strength (i.e., where $\cos \omega t = 1$), because of the phase difference between the instantaneous electric field strength and the imposed electric field [Eq. (4)]. Third, the frequency of oscillation of the drop is twice that of the initial imposed electric field.

The electrohydrodynamically induced fluid flow finds relevance in microfluidic applications involving enhancement of heat transfer rate [33] and fluid mixing [34,35]. Here, information about the relative importance of the characteristic time scales that control the flow field compared to the time scale of the process of interest is a key to the optimum design and performance of the microdevices. To gain insight into the strength of the flow field and its evolution with time, we have calculated the kinetic energy of the fluid,

$$\mathrm{KE} = \frac{1}{2} \int_A \rho |\mathbf{u}|^2 \mathrm{d}A, \tag{3}$$

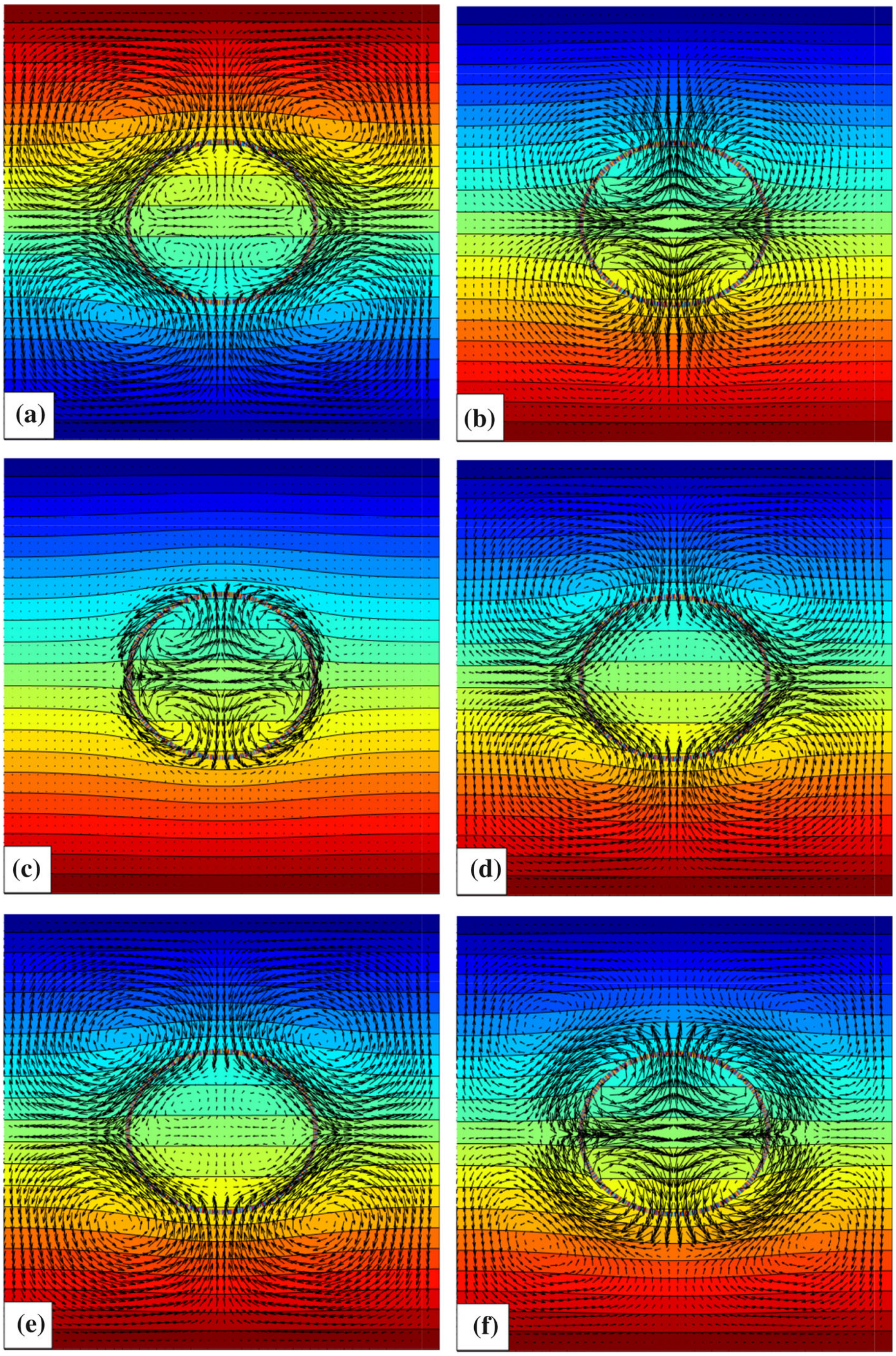

Fig. 6 Vector plot of the velocity field (at every fifth grid point) along with contours of the electric potential and the drop at selected times in the quasi-steady state, pertaining to the representative simulation for region **I**. The frames correspond to the markers in Fig. 4

where $A = WH$ is the area of the computational domain. The kinetic energy is scaled with $\rho_o u_s^2 A$, $u_s = \epsilon_o E_0^2 a/\mu_o$ being the electrohydrodynamic velocity scale. The time is nondimensionalized by the time scale of the electric field, $\tau_e = 1/\omega$.

Figure 7a shows the KE $-\, t$ curve, along with the corresponding curve for the DC field and the $\phi_t - t$ curve. In this Figure, we mark the KE $-\, t$ curve for the AC field by solid circles and the $\phi_t - t$ curve by solid squares at the times that correspond to the velocity snapshots. The kinetic energy goes through a transient period, which is

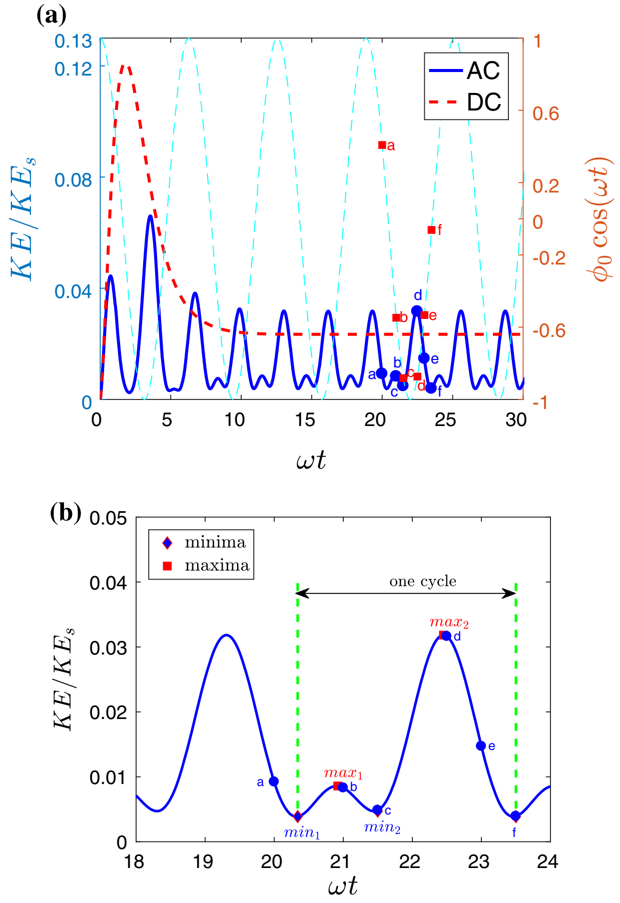

Fig. 7 Evolution of the kinetic energy of the fluid system with time [frame (a)], pertaining to simulation in Fig. 6. The red dashed line represents $KE - t$ for the corresponding DC field simulation. The solid circles and squares mark the $\mathcal{D} - t$ and $\phi_t - t$ curves, respectively, at the times that correspond to the times of the velocity snapshots. Frame (b) magnifies the part of frame (a) that is our focus

roughly the same as the deformation relaxation time τ, before it settles to its quasi-steady state. The frequency of oscillation of the kinetic energy is about 4ω, which is expectable since the frequency of oscillation of the velocity field is 2ω. At quasi-steady state, the $\mathrm{KE} - t$ curve has two maxima and two minima over a cycle (Fig. 7b). Here, the magnitudes of the two minima are essentially the same, while there is a sizable difference between the magnitudes of the two maxima. The kinetic energy during the rebound half-cycle [markers (a)–(c) on the curve] on average is smaller than that during the deformation half-cycle [markers (d)–(e) on the curve], which is intuitively understandable, since in the rebound process the electric pressure $[\![\tau^e_{nn}]\!]$ is relatively weak. Here, the minimum and the maximum kinetic energies correspond, respectively, to frames (c) and (d), where the drop deformation is minimum for frame (c) and around the mean for frame (d). This observation can be justified by noting that the fluid flow is the result of the drop deformation and the hydrodynamic shear, and therefore, the strength of the flow is controlled by these two components, i.e., $\mathbf{u} \sim \mathbf{u}_t + \mathbf{u}_n$. It should be noted, however, that for this dynamic problem (i.e., drop in an AC field), where the rate of the deformation $\partial\mathcal{D}/\partial t$ changes continuously, it is expected that the deformation-driven flow is stronger than that of the shear-driven one. Thus, the kinetic energy can be minimum when the rate of the deformation is minimum, which happens when the deformation is minimum or maximum. This seems to be the case here, considering Figs. 5 and 7, which show that the kinetic energy for frames (a), (c), and (f) is essentially minimum, where the deformation is nearly maximum or minimum. On the other hand, when the deformation is around the mean in the course of the deformation half-cycle, the rate of the deformation is maximum (in an absolute sense) and thus leads to a strong fluid flow.

Compared to the AC field, the kinetic energy of the DC field reaches a maximum in a relatively short time ($\omega\tau \sim 2.5$), corresponding to the time scale of diffusion of the momentum $\omega\tau_{\mathrm{diff}}$, and then settles to a steady state during a relaxation time ($\omega\tau \sim 8$) that is roughly the same as that for the deformation curve.

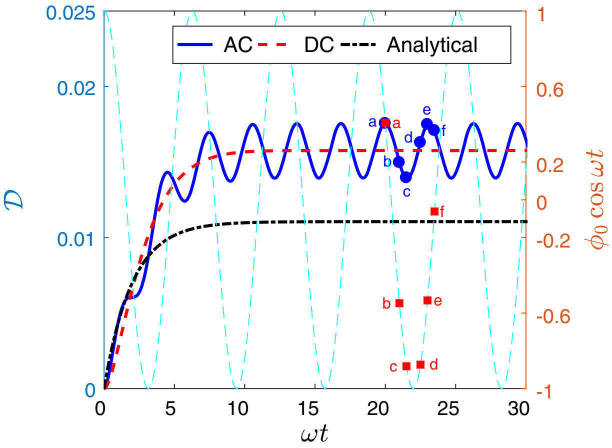

Fig. 8 Evolution of the deformation parameter $\mathcal{D}$ with time, pertaining to the representative simulation in region **II**. The red dashed line represents $\mathcal{D} - t$ for the corresponding DC field simulation. The dashed-dotted line is based on Eq. (15). The solid circles and squares mark the $\mathcal{D} - t$ and $\phi_t - t$ curves, respectively, at the times that correspond to the times of the velocity snapshots

Here, the kinetic energy in the DC field is larger than the perceived mean kinetic energy in the AC field in the quasi-steady state. This is because there is about a threefold reduction in the kinetic energy when the rate of deformation is minimum, compared to that when the deformation is around the mean.

5.3 Region **II** of the map

We now turn our attention to the evolution of the flow field and the drop for a representative fluid system in Region **II** of the map. Here, we expect the mean drop shape to be a prolate. Figure 8 shows the deformation–time for this case, where as before we have added the $\mathcal{D} - t$ curve, corresponding to the DC field simulation, along with the result of Eq. (15) to the Figure. The DC simulation corresponds to Fig. 3b. Comparison of the DC curves with the AC one leads to the same observation that was made earlier concerning the simulations in region **I**; namely, the DC numerical curve follows closely the perceived curve for the mean deformation in the AC field, and that the transient time for the total deformation ($\mathcal{D} = \mathcal{D}_m + \mathcal{D}_{tp}$) in the AC field, τ_{AC}, can be well estimated by Eq. (15). We note, however, that Eq. (15) leads to a larger underprediction of the steady-state deformation in the DC field, in comparison with the simulation in region **I**.

Figure 9 shows the velocity field. Here, $\widetilde{\sigma} = 6 < \widetilde{\epsilon} = 10$, and therefore, it is expected that the mean external flow runs from the poles toward the equator, as was the case for the previous simulation. As before, to facilitate the analysis, we concurrently consider the velocity field, Fig. 9, and the deformation–time history, Fig. 8. The velocity field for the first frame, which is essentially at the time of maximum deformation, is similar to that for the corresponding DC field (Fig. 3b), i.e., the external flow runs from the poles toward the equator. Here, frames (a), (c), and (e) correspond (nearly) to the times of maximum or minimum deformation. As such, the flow structure for these frames comprises closed vortices that are mostly confined within the drop or its surface. On the other hand, for frames (b) and (f), which reside in the rebound half-cycle, and frame (d), which resides in the deformation half-cycle, the sense of flow circulation is in line with the direction of the drop deformation. Specifically, in frames (b) and (f) where the poles move toward the center and the equator moves away from it, the fluid flow crosses into the drop at poles and exits at the equator, while for frame (d) the fluid flows in the opposite direction because of the reversal in the direction of motion of the drop surface.

The general feature of the kinetic energy–time curve (Fig. 10) is similar to that of the previous simulation (Fig. 7), i.e., the kinetic energy goes through a transient period and settles to a quasi-steady state. As before, the kinetic energy is maximum when the deformation is near the mean ($\mathcal{D}_m$) during the deformation half-cycle [marker (d) on the $\mathcal{D} - t$ curve], and it is minimum when the rate of the deformation is minimum [marker (a) on the $\mathcal{D} - t$ curve]. However, here the differences between the magnitudes of the two minima and the two maxima are, respectively, larger and smaller than the corresponding differences in the previous simulation, as can be seen by comparison of Figs. 7b and 10b. The evolution of the kinetic energy of the DC field is similar to that for the previous case. Furthermore, as before, the kinetic energy of the DC field at steady state is larger than the perceived mean kinetic energy of the AC field in the quasi-steady state.

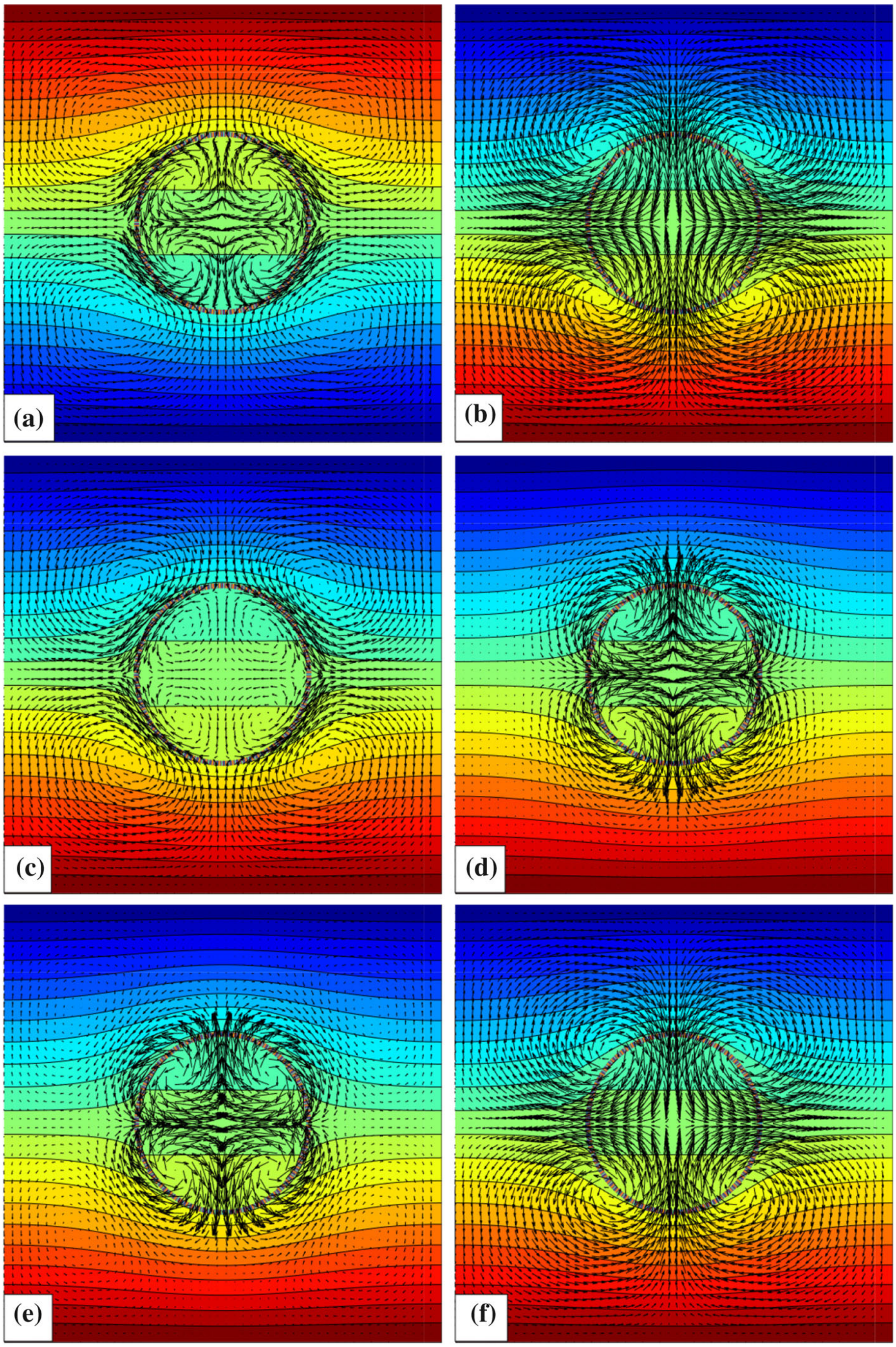

Fig. 9 Vector plot of the velocity field (at every fifth grid point) along with contours of the electric potential and the drop at selected times in the quasi-steady state, pertaining to the representative simulation in region **II**. The frames correspond to the markers in Fig. 4

5.4 Region **III** of the map

As a representative simulation in this region, we consider $\widetilde{\sigma} = 6 > \widetilde{\epsilon} = 2$. Therefore, the time-independent external flow will run from the equator to the poles, which is in the opposite direction to that in the previous two cases. Furthermore, $\Phi_m > 0$, and therefore the drop will become prolate. Figures 11, 12, and 13 present the pertinent results. Here, the evolution of the flow field (Fig. 12) is in many ways similar to that for the first

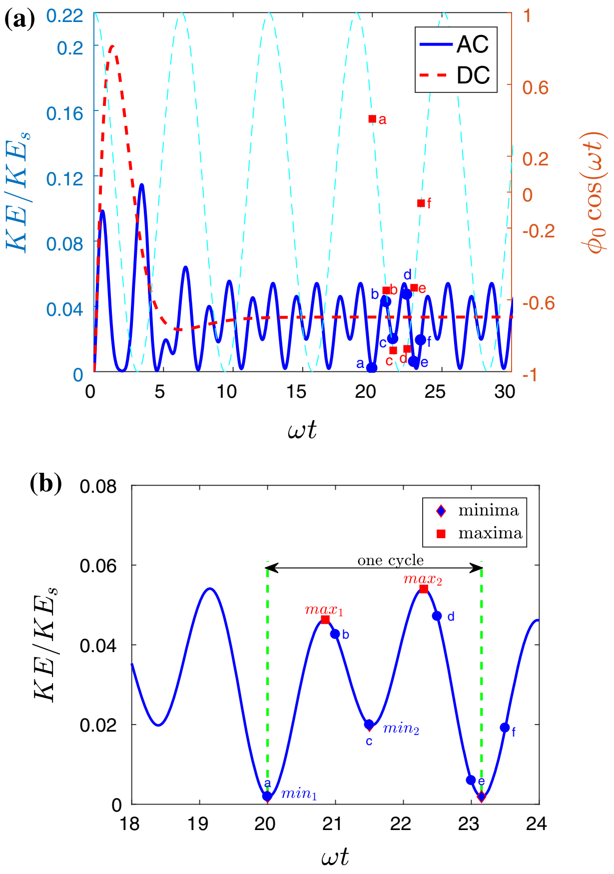

Fig. 10 Evolution of the kinetic energy of the fluid system KE with time [frame (a)], pertaining to simulation in Fig. 9. The red dashed line represents KE $-\ t$ for the corresponding DC field simulation. The solid circles and squares mark the $\mathcal{D}-t$ and ϕ_t-t curves, respectively, at the times that correspond to the times of the velocity snapshots. Frame (b) magnifies the part of frame (a) that is in our focus

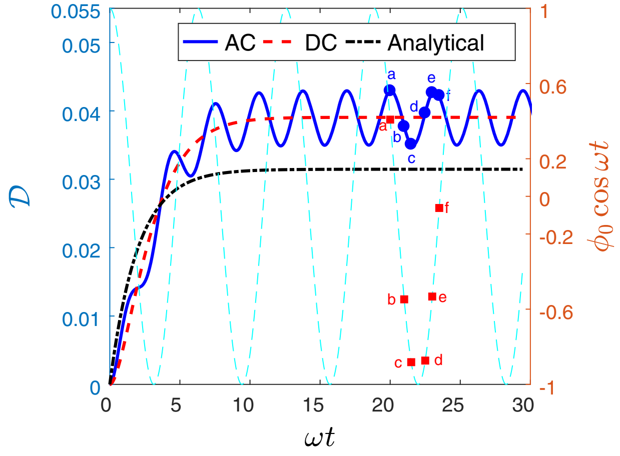

Fig. 11 Evolution of the deformation parameter $\mathcal{D}$ with time, pertaining to the representative simulation in region **III**. The red dashed line represents $\mathcal{D}-t$ for the corresponding DC field simulation. The dashed-dotted line is based on Eq. (15). The solid circles and squares mark the $\mathcal{D}-t$ and ϕ_t-t curves, respectively, at the times that correspond to the times of the velocity snapshots

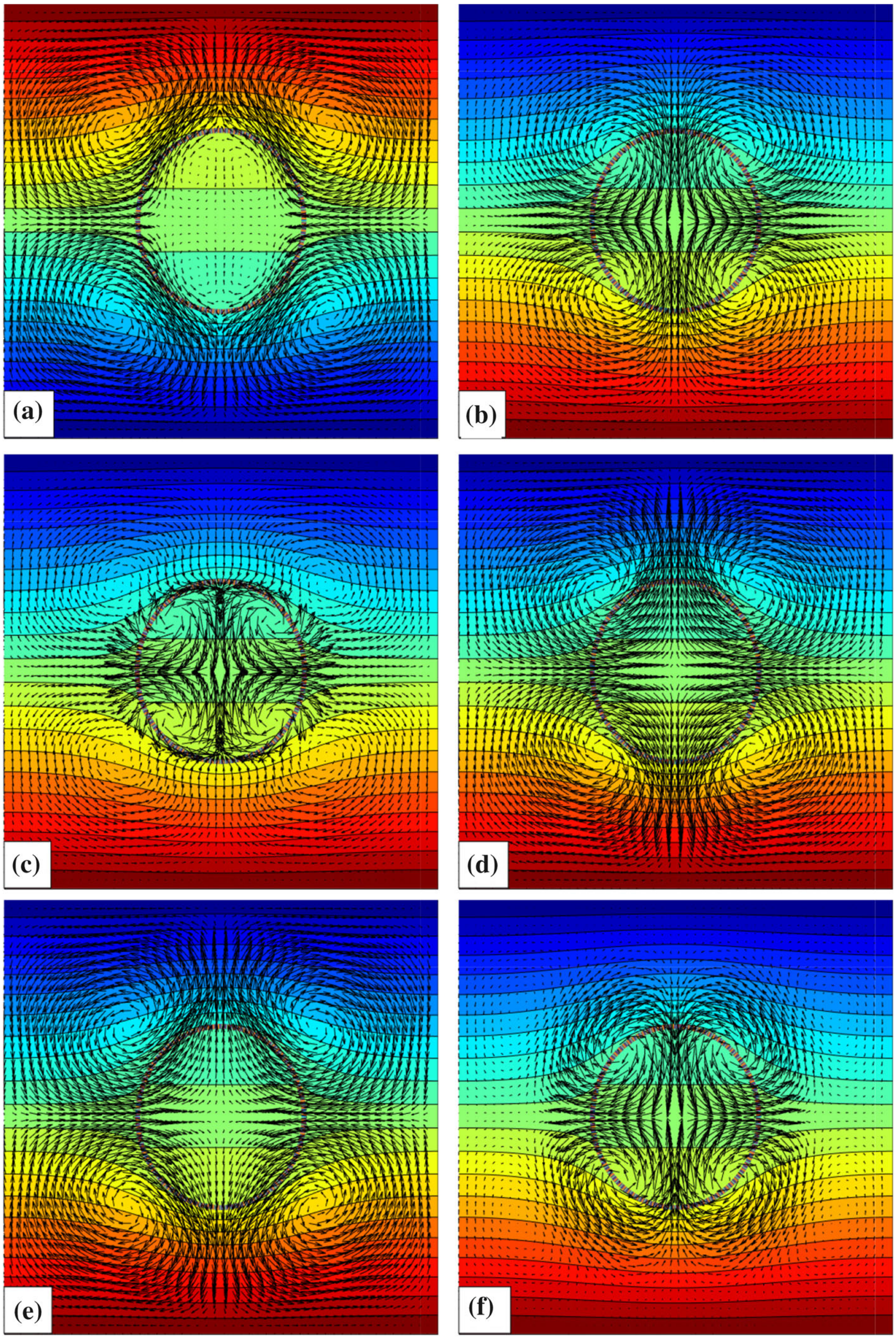

Fig. 12 Vector plot of the velocity field (at every fifth grid point) along with contours of the electric potential and the drop at selected times in the quasi-steady state, pertaining to the representative simulation in region **III**. The frames correspond to the markers in Fig. 4

case, Fig. 6, with the only difference that the direction of the flow is opposite. The general features of the $\mathcal{D}-t$ and $\mathrm{KE}-t$ curves are similar to those of the corresponding curves for the previous two simulations. The minimum kinetic energy corresponds to the state of minimum or maximum deformation, and the maximum kinetic energy corresponds to the mean ($\mathcal{D}_m$) deformation during the deformation half-cycle. On the other hand, here the difference in magnitudes of the two minima is larger than that for the first simulation, but is smaller than that for the second simulation, and the difference in magnitudes of the two maxima is larger than that

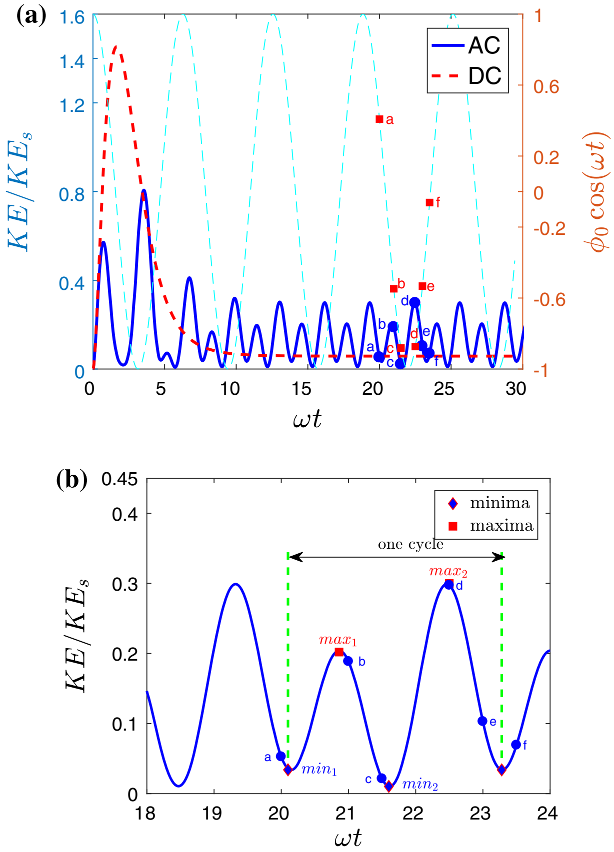

Fig. 13 Evolution of the kinetic energy of the fluid system KE with time [frame (a)], pertaining to simulation in Fig. 12. The red dashed line represents KE $-\,t$ for the corresponding DC field simulation. The solid circles and squares mark the $\mathcal{D}-t$ and $\phi_t - t$ curves, respectively, at the times that correspond to the times of the velocity snapshots. Frame (b) magnifies the part of frame (a) that is in our focus

for the first and the second simulations; see Figs. 7b, 10b, and 13b. Interestingly, however, the kinetic energy from the corresponding DC simulation appears to be lower than the mean kinetic energy in the quasi-steady state. This is presumably because of a higher rate of disturbance that is produced in this case, as a result of drop oscillation.

6 Confinement effect

In the course of comparison of the numerical and the analytical deformations of a drop in a DC electric field it was observed that the analytical solution underpredicted the numerical results for all of the three fluid systems. This discrepancy was conjectured to be due to the confinement and inertia effects, which were present in the numerical simulation, but were absent in the analytical one. Specifically, in the numerical simulation the area fraction was $\alpha = 0.1256$ and the flow Reynolds number was $Re_f = 1$, as opposed to $\alpha \ll 1$ and $Re_f \ll 1$ in the analytical solution. To explore this issue further, we have modified Eq. (15) by replacing the deformation $\mathcal{D}$ with that predicted by Ref. [32, Eq. (17)]. These authors accounted for the confinement effect by considering a drop of radius a in the center of a circular channel of radius b, where the channel wall was imposed to a uniform electric field strength of E_0. Accordingly, the deformation was found to be

$$\mathcal{D} = \frac{1}{3} Ca_f \Gamma^2 \Phi_C \tag{17}$$

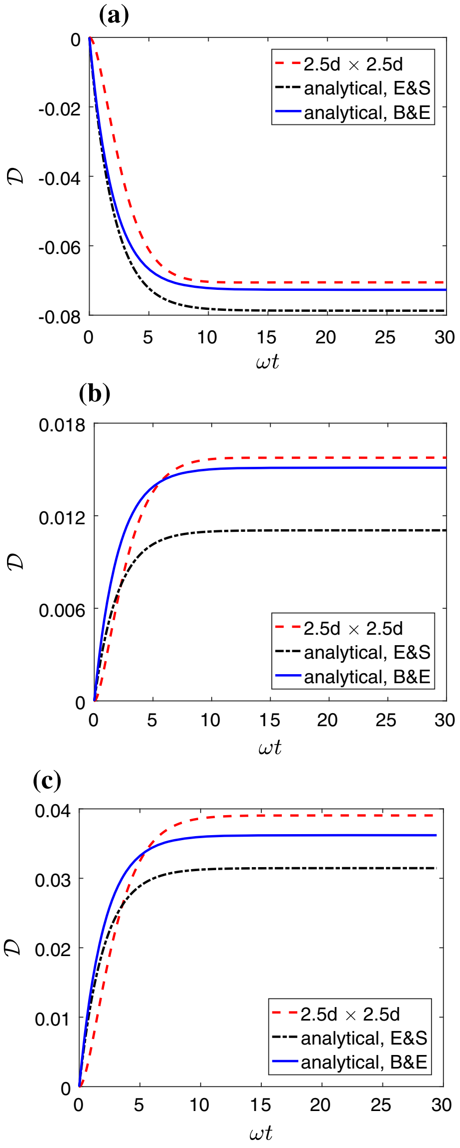

Fig. 14 Effect of the confinement on the drop deformation for representative fluid systems in regions **I–III**, corresponding to frames (a)–(c), respectively. The $E\&S$ solution, Eq. (15), is for a drop in an unbounded domain, while the $B\&E$ solution, Eq. (17), accounts for the confinement effect

where

$$\Phi_C = \frac{\tilde{\sigma}^2+1-2\tilde{\sigma}+\mathcal{F}(\tilde{\sigma}-\tilde{\epsilon})}{(\tilde{\sigma}+1)^2}, \tag{18.1}$$

$$\Gamma = \frac{\tilde{\sigma}+1}{(\tilde{\sigma}+1)-\lambda^2(\tilde{\sigma}-1)}, \tag{18.2}$$

$$\mathcal{F} = \frac{(\lambda^2-1)^2\tilde{\mu}-(\lambda^4+6\lambda^2-1)}{(\lambda^2-1)^2\tilde{\mu}+(1-\lambda^4)}. \tag{18.3}$$

Here, Φ_C is the deformation characteristic function, Γ and $\mathcal{F}$ are correction factors that take into account the effect of confinement on the electric field and the fluid flow, respectively, and $\lambda = a/b$ is the confinement parameter. For $\lambda = 0$, Eq. (17) converges to Eq. (12).

Figure 14 shows the comparison of the deformations from the numerical simulations (Fig. 3) with the predictions of Eqs. (12) and (17). As is evident, accounting for the confinement effect in the analytical equation leads to a better agreement between the analytical and the numerical results, with the residual difference being due to the inertia effect.

7 Conclusions

Electrohydrodynamics of a liquid drop in uniform AC electric fields was studied using direct numerical simulations (DNS). A front-tracking/finite difference method was used in conjunction with Taylor–Melcher's leaky dielectric model to solve the governing electrohydrodynamic equations. Representative simulations for the three regions of the deformation–circulation map were performed at low electric frequency. The evolution of the drop deformation $\mathcal{D}$ with time t showed that the drop settled to its quasi-steady state in a relaxation time τ that was set by the viscous and the capillary force. For the range of the input parameters used in this study, the mean drop deformation was the same as the deformation of the drop in the corresponding DC field in an rms sense. The evolution of the flow field showed formation of closed vortices that crossed the drop surface with a sense of circulation that was in line with the direction of motion of the drop surface. The flow pattern was the same as that for a drop in the steady-state DC field, corresponding to the maxima and minima of the $\mathcal{D} - t$ curve, where the rate of the deformation $(\partial\mathcal{D}/\partial t)$ was zero. The evolution of the kinetic energy of the fluid system with time was investigated, and it was shown that in general the minimum kinetic energy corresponded to the state of minimum or maximum deformation, where the rate of the deformation $(\partial\mathcal{D}/\partial t)$ was zero. The maximum kinetic energy, on the other hand, corresponded to the state of mean (time-independent) deformation during the deformation half-cycle, where the rate of the deformation was maximum.

References

1. Wang, Q., Suo, Z., Zhao, X.: Bursting drops in solid dielectrics caused by high voltages. Nat. Commun. **3**, 1157 (2012)
2. Eow, J.S., Ghadiri, M.: Electrostatic enhancement of coalescence of water droplets in oil: a review of the technology. Chem. Eng. J. **85**(2), 357–368 (2002)
3. Kim, H., Luo, D., Link, D., Weitz, D.A., Marquez, M., Cheng, Z.: Controlled production of emulsion drops using an electric field in a flow-focusing microfluidic device. Appl. Phys. Lett. **91**(13), 133106 (2007)
4. Taylor, G.: Studies in electrohydrodynamics: I. the circulation produced in a drop by an electric field. Proc. R. Soc. A **291**, 159–167 (1966)
5. Smith, C., Melcher, J.: Electrohydrodynamically induced spatially periodic cellular Stokes-flow. Phys. Fluids **10**, 2315–2322 (1967)
6. Melcher, J.R., Taylor, G.I.: Electrohydrodynamics: a review of the role of interfacial shear stresses. Ann. Rev. Fluid Mech. **1**, 111–147 (1969)
7. Saville, D.A.: Electrohydrodynamics: the Taylor-Melcher leaky dielectric model. Ann. Rev. Fluid Mech. **29**, 27–64 (1997)
8. Torza, S., Cox, R.G., Mason, S.G.: Electrohydrodynamic deformation and burst of liquid drops. Philos. Trans. R. Soc. A **269**(1198), 295–319 (1971)
9. Vizika, O., Saville, D.: The electrohydrodynamic deformation of drops suspended in liquids in steady and oscillatory electric fields. J. Fluid Mech. **239**, 1–21 (1992)
10. Baygents, J., Rivette, N., Stone, H.: Electrohydrodynamic deformation and interaction of drop pairs. J. Fluid Mech. **368**, 359–375 (1998)
11. Moriya, S., Adachi, K., Kotaka, T.: Deformation of droplets suspended in viscous media in an electric field. 1. Rate of deformation. Langmuir **2**(2), 155–160 (1986)
12. Moriya, S., Adachi, K., Kotaka, T.: Deformation of droplets suspended in viscous media in an electric field. 2. Burst behavior. Langmuir **2**(2), 161–165 (1986)
13. Nishiwaki, T., Adachi, K., Kotaka, T.: Deformation of viscous droplets in an electric field: poly (propylene oxide)/poly (dimethylsiloxane) systems. Langmuir **4**(1), 170–175 (1988)
14. Limat, L., Stone, H.A., Viovy, J.L.: Electrohydrodynamic stability of a liquid column under cross fields: application to continuous flow electrophoresis. Phys. Fluids **10**(10), 2439–2450 (1998)
15. Taylor, G.: Disintegration of water drops in an electric field. Proc. R. Soc. Lond. A Math. Eng. Sci. **280**(1382), 383–397 (1964)
16. Allan, R., Mason, S.: Particle behaviour in shear and electric fields. I. Deformation and burst of fluid drops. Proc. R. Soc. Lond. A Math. Phys. Eng. Sci. **267**(1328), 45–61 (1962)
17. Sozou, C.: Electrohydrodynamics of a liquid drop: the time-dependent problem. Proc. R. Soc. Lond. A Math. Phys. Eng. Sci. **331**(1585), 263–272 (1972)
18. Thaokar, R.: Dielectrophoresis and deformation of a liquid drop in a non-uniform, axisymmetric AC electric field. Eur. Phys. J. E Soft Matter Biol. Phys. **35**(8), 1–15 (2012)
19. Behjatian, A., Esmaeeli, A.: Flow patterns and deformation modes of coaxial liquid columns in transverse electric fields. Eur. Phys. J. E Soft Matter **36**(10), 1 (2013)
20. Behjatian, A., Esmaeeli, A.: Transient electrohydrodynamics of a liquid jet: evolution of the flow field. Fluid Dyn. Mater. Process. **10**(3), 29–317 (2014)
21. Behjatian, A., Esmaeeli, A.: Equilibrium shape and hysteresis behavior of liquid jets in transverse electric fields. J. Electrostat. **75**, 5–13 (2015)

22. Tryggvason, G., Bunner, B., Esmaeeli, A., Juric, D., Al-Rawahi, N., Tauber, W., Han, J., Nas, S., Jan, Y.J.: A front-tracking method for the computations of multiphase flow. J. Comput. Phys. **169**(2), 708–759 (2001)
23. Halim, M.A., Esmaeeli, A.: Computational studies on the transient electrohydrodynamics of a liquid drop. FDMP Fluid Dyn. Mater. Process. **9**(4), 435–460 (2013)
24. Esmaeeli, A.: Dielectrophoretic-and electrohydrodynamic-driven translational motion of a liquid column in transverse electric fields. Phys. Fluids **28**(7), 073306 (2016)
25. Feng, J.Q.: Electrohydrodynamic behaviour of a drop subjected to a steady uniform electric field at finite electric Reynolds number. Proc. R. Soc. Lond. A Math. Phys. Eng. Sci. **455**(1986), 2245–2269 (1999)
26. Lanauze, J.A., Walker, L.M., Khair, A.S.: The influence of inertia and charge relaxation on electrohydrodynamic drop deformation. Phys. Fluids **25**(11), 484 (2013)
27. Das, D., Saintillan, D.: A nonlinear small-deformation theory for transient droplet electrohydrodynamics. J. Fluid Mech. **810**, 225–253 (2017)
28. Esmaeeli, A., Halim, M.A.: Electrohydrodynamics of a liquid jet in transverse AC electric fields. Int. J. Multiphase Flow **7**, 1037 (2018)
29. Rhodes, P.H., Snyder, R.S., Roberts, G.O.: Electrohydrodynamic distortion of sample streams in continuous flow electrophoresis. J. Colloid Interface Sci. **129**(1), 78–90 (1989)
30. Reddy, M.N., Esmaeeli, A.: The EHD-driven fluid flow and deformation of a liquid jet by a transverse electric field. Int. J. Multiphase Flow **35**, 1051–1065 (2009)
31. Esmaeeli, A., Sharifi, P.: The transient dynamics of a liquid column in a uniform transverse electric field of small strength. J. Electrostat. **69**(6), 504–511 (2011)
32. Behjatian, A., Esmaeeli, A.: Electrohydrodynamics of a liquid column under a transverse electric field in confined domains. Int. J. Multiphase Flow **48**, 71–81 (2013)
33. Kaji, N., Mori, Y., Tochitani, Y.: Heat transfer enhancement due to electrically induced resonant oscillation of drops. J. Heat Transfer **107**(4), 788–793 (1985)
34. Ward, T., Homsy, G.: Chaotic streamlines in a translating drop with a uniform electric field. J. Fluid Mech. **547**, 215–230 (2006)
35. Christov, C., Homsy, G.: Enhancement of transport from drops by steady and modulated electric fields. Phys. Fluids **21**(8), 083102 (2009)